A Low-Cost Digital Torquemeter Coordinated by Arduino Board

S. N. Ashwindran[1], A. A. Azizuddin[1*], A. N. Oumer[1]

[1]Faculty of Mechanical and Automotive Engineering Technology,
 Universiti Malaysia Pahang, Pekan, 26600, MALAYSIA

*Corresponding Author

Abstract: Torquemeter is a transducer for measuring rotational force and converting it into electronic output signal. In this paper, the techniques to fabricate a low cost yet effective torquemeter system is introduced. The device is calibrated and tested to prove it effectiveness and robustness. The system is developed to investigate the torque generated by wind turbine system. The presented torquemeter system comprises of two subsystems namely photointerrupter (primary) and load cell (secondary). The reliability of the developed system is analyzed by stages in order to verify the effectiveness in acquiring measurement namely RPM, weight (load) and torque. It is found that 5 kg load cell illustrated unsteady noise behavior relative to the defined calibration weight. Meanwhile, the percentage of accuracy (P_a) of final 3th reading is P_a = 94.709 %, 97.32 %, 98.826 % for 10 g, 20 g and 100 g respectively. Measurement acquired from torquemeter system is compared against 2D CFD numerical model under similar flow condition. Results shows that the measurement of torquemeter system is M_t = 0.731842 and as for CFD model is M_t = 0.82553 which results in error (%) of P_e = 11.35 %. However, the CFD numerical model has overpredicted moment value since it has compensated the blockage factor and external environmental factors. It is safe to say, that the presented instrument is applicable and feasible for WT torque acquisition.

Keywords: Torquemeter, arduino board, photointerrupter, load cell, strain gauge, wind tunnel, wind turbine

1. Introduction

Experimental fluid dynamics (EFD) is a research methodology to conduct investigation of scaled model or prototype in realistic environment and conditions. Information gained from EFD procedure help researchers to develop numerical models for system based simulations [1]. Experimental fluid dynamics are classified into two types namely concept-based experiments and data-based experiments [2]. Data-based experiments are conducted to document results on engineering design such as aerofoil series. The catalogued results are utilized for research method evaluation and improvement in order to develop numerical method for flow related methods and calculations. As for concept-based experiments, this method is based on the concept of analytically investigating the correlation within the mechanism of study for the purpose of discovering concepts. Hashimoto et al., (2019) [3] mentioned that standard complying high quality EFD data is crucial as it is utilized for the purpose for qualitative validation of CFD codes. Experiments provides motion for the development of theoretical studies, numerical modelling and simulations [4]. Experiments has played an important role for development of knowledge in fluid mechanics. Case in point, most of the fundamental aspects of fluid mechanics are contributed by infamous experiments conducted by researchers such as Archimedes principle [5]–[7], Reynolds number (*Re*) [8]–[10], Pascal principle [11], Torricelli mercury barometer [12]–[14] and

others. However, there are limitations to lab-based experiments in comparison to field experiment. Since the experimental procedure are conducted in controlled environment and conditions. Field experiments encapsulates the actual scenario where various unsteady variables and parameters influences the data collected [15]. Moreover, the magnitude of disturbance in field experiments are higher compare to lab-based experiments. Therefore, considering numerous variables and parameters at every level for a case study would be impossible. Hence, conducting research under controlled environment by considering selected crucial variables under proper assumption would be adequate for an experiment. van Riesen et al. (2019) [16] stated that by utilizing control of variables strategy (CVS) method, researcher is able to investigate experiments by considering selected variables are dependent and rest are kept constant.

Although lab-based experiments are not as accurate as field-based experiments, under proper assumption and conditions the percentage of error is trivial. Lab based experimental procedure requires standardized industrial grade instrument and equipment for data acquisition and analysis in which is costly. However, properly fabricated and well calibrated instrument is cost effective in contrast to purchase high end industrial grade scientific instrument. The aim of this study is to develop a low-cost torquemeter coordinated by Arduino board. In this study the reliability of the developed system is analyzed by stages in order to verify the effectiveness in acquiring the moment properties of wind turbine (WT) in wind tunnel (WTL) environment.

2. Literature Review

Instruments in WTL facility is subject to the scope and objective of the investigation namely auxiliary mechanical behavior data acquisition system [17]–[19], flow visualization [20]–[22], fluid flow factors [23], [24] and WTL flow condition [25], [26]. Instruments such as torque transducer [27], [28], pressure transducer [29], [30] and strain-gauge sensor or load cell [31]–[33] is required to investigated the properties of a body influence under flow. There are two types of torque meter namely reaction (static) and rotary (dynamic or rotational). Torque sensors are classified into different types with respect to their measuring principal namely direct and indirect [34]. The physics behind the mechanism of torque sensor is that the transducer is composed of strain gauge which converters mechanical force into electrical signals as shown in Fig. 1 (a). In other words, the system converts strain incurred by mechanical load namely tension, compression, weight, force and torque into electrical resistance. Conventionally in wind turbine investigation, torque transducer namely rotary torque sensor (dynamic torque sensor) is utilized to measure the rotation torque of WT shaft as shown in Fig. 1 (b). Zappalá et al., (2018) [35] stated that the relationship between the torque generated by the rotating WT shaft and relative rotation located at the end of the shaft section is descripted in Equation 1. Where I is moment of inertia (kg m^2), C represents shaft damping coefficient (kg m^2 s^{-1} rad^{-1}) and K is shaft torsional stiffness (N m rad^{-1}).

$$T = I\ddot{\theta} + C\dot{\theta} + K\theta \qquad (1)$$

However, standard industrial grade torque transducer is expensive and requires expertise in maintenance and installation. Although, standard torque transducer is accurate and sensitive in acquiring data, price of the instrument out ways the benefit. Therefore, self-fabrication from scratch is much more self-sufficient and cost effective oppose to off the shelf instruments. In respect of wind turbine torque measurement there are two old and less prominent methodology namely Prony brake system [36] and deriving reaction force form bearing [37]. Although there are several configurations to torquemeter, the working principal of this instruments are based on Prony brake or friction dynamometer mechanism. Mechanism inspired by Prony brake system can be classified into two types namely mechanical system and digital microcontroller. Although, digital microcontroller is costly, the accuracy and precision of a well calibrated digital system is higher than mechanical system. Commonly, WTL facility specialized for the study WT is equipped with torque sensor. However, in absence of standard torque meter can be compensated with low-cost torque meter based on Arduino microcontroller.
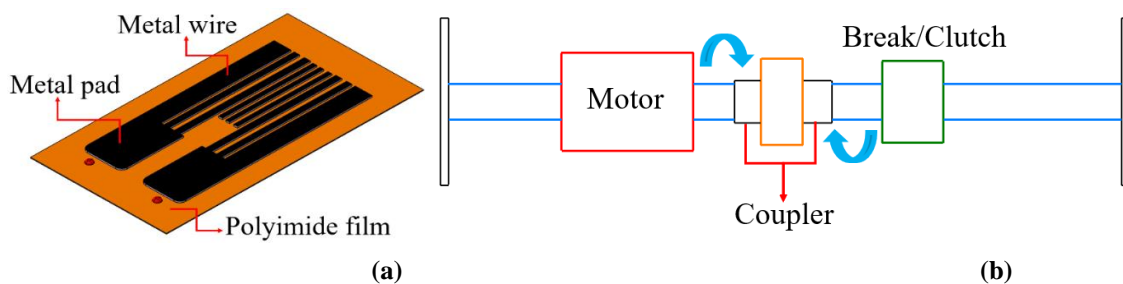

Fig. 1 - Torque trasnduser (a) dynamic torque meter mechanism; (b) metal foil strain gauge

3. Methodology

As illustrated in Fig. 2, the WT system constructed for WTL experimental procedure. The system consists of 7 elements namely load cell, photointerrupter, friction clamp, WT blade, shaft, double gap flywheel and RS 775 DC motor (load). The shaft of the WT is attached to a support structure which is imposed with the upper surface of the test section. The shaft of the WT rotor is a hollow brass tube with uniform circular cross section and linear homogenous elastic material. The outer diameter (OD) of the brass shaft 6.2 mm. However, due to the variance in diameter of the rotor shaft and DC motor shaft, a 3D printed female straight tube connector is utilized to attach both of the items. The parts are 3D printed with high pression relative to their fittings and dimension in order to avoid disengagement and loose fitting which consequently impact the performance of the turbine. Moreover, additional reinforcement has been imposed namely adhesive glue and tape to strengthen the inter bonding of the components. DC motor with capability of 8000 RPM is utilized in order to cater the relative rotation of the WT that is subjected to constant wind load ranging from 5.0 m/s to 7.0 m/s. Additional auxiliary components are required in order to achieve the torque meter system as illustrated in Fig. 2. The auxiliary components are friction clamp, connector, and double gap flywheel. However, due to components required to construct the torque meter, approximately an additional 3 % of blockage ratio is subjected to the WT system. Hence the final blockage ratio of the WT system which is the cumulative of the projected area of the WT blade and torque meter components is $B_r = 21.6$ %.
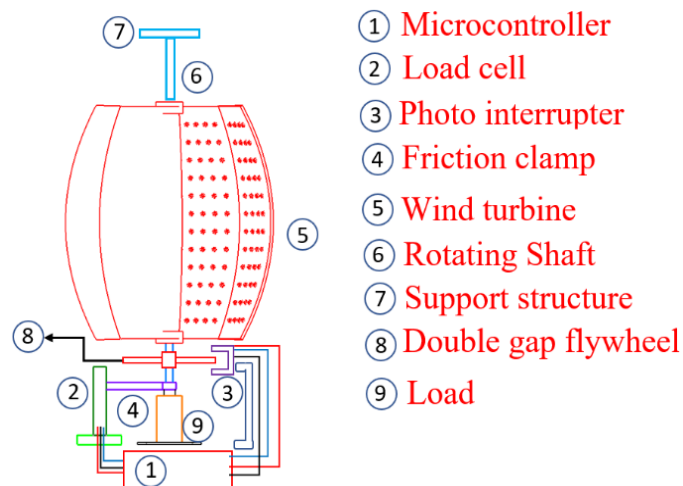

1. Microcontroller
2. Load cell
3. Photo interrupter
4. Friction clamp
5. Wind turbine
6. Rotating Shaft
7. Support structure
8. Double gap flywheel
9. Load

Fig 2 - Illustration of WT configuration in WT experimental procedure

The fabricated torque meter consists of two subsystems namely photointerrupter (primary) and load cell section (secondary) coordinated by Arduino Mega 2560. The role of the primary section of the torque meter is to measure the RPM generate by the WT. Photo interrupters are non-contact optical components which outperforms mechanical switches in terms of reliability and avoids abrasion due to wear and tear [38]. The utilized photointerrupter is standard manufactured component with part ID of GP1A57HRJ00F. This photointerrupter has five pins with gap of 10 mm and slit width of 1.8 mm as shown in Fig. 3 (a). The photointerrupter consist of namely emitter and detector in straight and aligned configuration. The emitter consists of infrared (IR) LED with a forward voltage drop of ± 1.2 V along with 10 mA – 20 mA. The emitted light is then received by the optical sensor (detector), where the signal is amplified with Schmitt trigger. The voltage drops the instant optical path is blocked indicating an obstacle as illustrated in Fig. 3 (b). Conventionally, picket fence tape or photogate tape [39] is recommended in order for the optical sensor to differentiate opaque and transparent zone. However, motion subjected to rotation, flywheel with tab or gap or spoked wheel is required to differentiate the zones of the flywheel and to uniformly interrupt the optical sensor for steady output. In this scenario, 3D printed double gap flywheel is utilized as the obstacle factor for photointerrupter system. As manifested in Fig. 4, the double gap flywheel is attached to the connector, where it is aligned between the emitter and receiver of the photointerrupter. The role of photointerrupter subsystem is to act as a digital tachometer to measure the RPM of the rotating WT shaft. In order to reduce the number of components and blockage ratio induced by the auxiliary component of the torque meter system, in this study breakout board is utilized instead of breadboard. Breakout boards is a printed circuit board (PCB) with properly spaced pinhole for sensor and IC which provides a straightforward electrical circuit configuration. In this research, photointerrupter breakout board with ID of GP1A57HRJ00F. The breakout board has three additional pins holes namely power, signal and ground which replace the use of breadboard and terminals or chocolate block connector. In conjunction to interface breakout board and photointerrupter, a 220 Ω resistor is required.

Since it is noted that the operating voltage is ranging from 3.3 v to 5V interfaced photointerrupter is connected to Arduino pinned at ground, power (5 V) and A8 analog input pin. The interfaced photointerrupter system with Arduino is then tested with execution code acquired from Sparkfun. Since the utilized Arduino code is a simple code command based on "All clear" and "Gate obstructed" indicated in Arduino serial monitor. However, the photointerrupter system did not detect the 3D printed double gap flywheel as an obstacle indicating all clear via serial monitor. In regards to several research community forums, it is said that polylactic acid (PLA) is transparent to low frequency infrared spectrum. Therefore, double gap flywheel is layered with aluminum tape. Photointerrupter infrared system detected the presence and interruption of aluminum taped double gap flywheel. Initial testing reveal that the thickness of the PLA based double gap flywheel impacts the performance of the photointerrupter subjected to the penetration intensity of infrared spectrum. Since the photointerrupter system is dubbed as digital tachometer system, the operating code is constructed in regards to acquire RPM data of the WT relative to the motion of the double gap flywheel. The acquired RPM data from photointerrupter system is validated against values obtained from non-contact UNI-T UT 373 digital tachometer. Table 1 shows average RPM data of WT via UNI-T UT 373 digital tachometer and photointerrupter system at different wind speed ranging from 5.1 m/s, 5.3 m/s and 5.9 m/s.
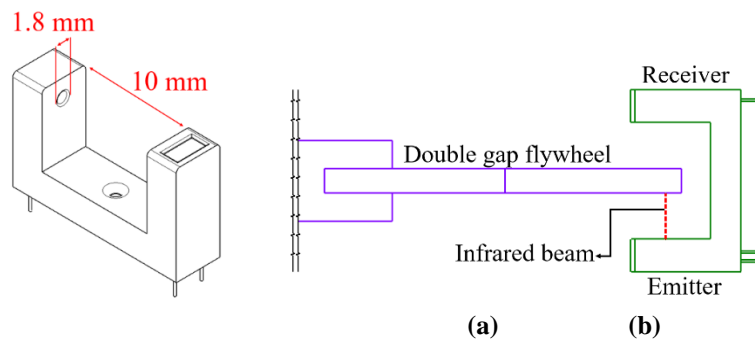
Fig. 3 - Photointerrupter mechanism (a) photointerrupter; (b) photointerrupter infrared working mechanism
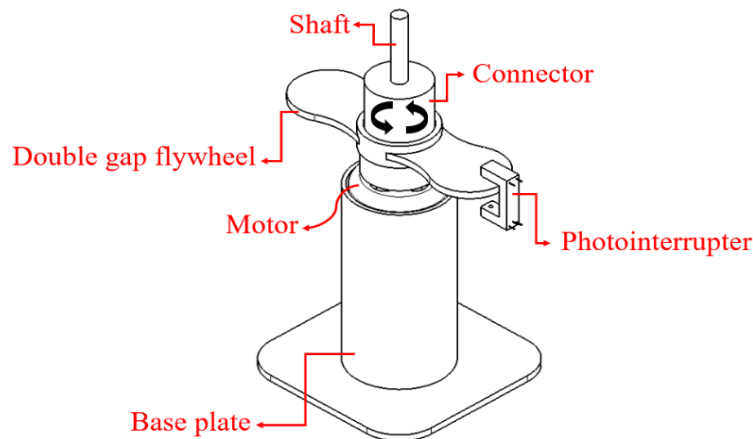
Fig. 4 - Illustration of double gap flywheel and photointerrupter susbsytem relative to WT system

Table 1 - RPM values of photointerrupter system and tachometer

Wind speed (m/s)	Photointerrupter system (RPM)	Tachometer (RPM)
5.1	325	342
5.3	359	371
5.9	404	419

The secondary part of the torque meter is the load cell system, which is composed of straight bar load cell and HX711 amplifier. Load cell is composed of transducer that converts the applied load (force) into electrical signal [40]–[42]. In other words, the load cell changes its electrical resistance relative to its deformation subjected to the force applied. The change in electrical signal induced by deformation of the load cell strain gauge which is then amplified by HX711 [43]. In addition, HX711 is an analog to digital converter (ADC) with precision of 24-bit. In this study, load cells rated capacity of 5 kg and 20 kg with part ID of TAL 220B and TAL 220 respectively is utilized in order to obtain

the appropriate nominal range load cell for the WT system under the influence of wind load ranging from 5.0 m/s to 7.0 m/s. The load cell utilizes four wire Wheatstone bridge configuration in order to interface with HX711 namely Red, Yellow, Green, White and Black. Moreover, HX711 has another four-wire interface for Arduino microcontroller namely ground, voltage common collector (VCC), data and clock. However, the interfaced load cell and HX711 system coordinated by Arduino need to be verified and calibrated. Although, there are several calibration techniques that differs with respect to the type of load cell, the conventional method for strain gauge load cell is to utilized slot weight or cylindrical weight. The purpose of the weight is to calibrate the load cell to the exact known load relative to the weight utilized. Moreover, via this technique information on sensitivity and linearity of strain gauge load cell is obtained with regards to the rated capacity of 5 kg and 20 kg.

In regards to the adapted calibration technique, one end of the straight bar load cell is clamped via G-clamp resembling cantilever beam configuration. It is noted that, the orientation of the load cell in regards to the applied load is crucial in calibration and accuracy of the measurement. Conventionally, for single point strain gauge load cell adhesive label is attached on the surface of the load cell indicating the direction of the deflection. However, it is found that for 20 kg load cell is not presented with recommended flex direction label. Therefore, the top and bottom of the load cell surface relative to the tapped screw hole is subjected to load in order to obtain the deflection direction namely positive or negative. The appropriate orientation of the load cell indicated positive output, where else incorrect installation indicates negative load measurement. The framework of the calibration code is composed of 2 sections namely tare and calibrated mass. Since the calibration technique utilized known mass value, this ensures the appropriate approximation for the force applied on the load cell. The structure of the calibration code is based on equation of line relative to load cell and HX711 as shown in Equation 2. Relative to equation of line, x represents ADC HX711 reading and y is known mass, m is calibration line slope and d stands for the intercept at $y = 0$ which is at absence of mass or accounted as tare point. Meanwhile (x_0, y_0) and (x_1, y_1) is considered as dummy points for the slope as shown in Equation 3 - Equation 4. Relative to d, Equation 6 is derived from slope gradient of calibration (k) Equation 5. Since two known mases is utilized the expression for calibration line or factor is shown in Equation 7. Since, the initial mass namely $y_0 = 0$, the simplified and final expression is shown in Equation 8.

Equation of line,

$$y = kx + d \tag{2}$$

Equation of line relative to dummy points,

$$y_0 = kx_0 + d \tag{3}$$

$$y_1 = kx_1 + d \tag{4}$$

Slope gradient of calibration line, k,

$$k = \frac{y_1 - y_0}{x_1 - x_0} \tag{5}$$

Intercept d,

$$y_0 = \left(\frac{y_1 - d}{x_1} \right) x_0 + d$$

$$y_0 x_1 = (y_1 - b) x_0 + x_1 d$$

$$y_0 x_1 - y_1 x_0 = (x_1 - x_0) d$$

$$d = \frac{y_0 x_1 - y_1 x_0}{x_1 - x_0} \tag{6}$$

Definition for calibration line via known mases,

$$y = \left(\frac{y_1 - y_0}{x_1 - x_0} \right) x + \left(\frac{y_0 x_1 - y_1 x_0}{x_1 - x_0} \right) \tag{7}$$

Calibration expression subjected $y_0 = 0$,

$$y = \left(\frac{y_1}{x_1 - x_0} \right) x + \left(\frac{y_1 x_0}{x_1 - x_0} \right)$$

$$y = \left(\frac{y_1}{x_1 - x_0} \right) (x - x_0) \tag{8}$$

The load cells of rated capacity of 5 kg and 20 kg is then tested at two different loads namely 5 g and 50 g over time period of 60 s. Fig. 5 (a) and Fig. 5 (b) shows the reading gathered via 5 kg load cell relative to 5g weight for 60 s. Meanwhile, Fig. 5 (c) shows the reading gathered via 20 kg load cell relative to 50 g weight for 60 s. It is found that with the 20 kg load cell is insensitive to 5 g. This due to the low load of 5 g which is not sufficient for the deformation or deflection of the strain gauge. Results shows that 5 kg load cell is sensitive to wider range of load in contrast to 20 kg load cell. The average calibration weight acquire by 5 kg load cell with load of 5 g is W = 4.987, where else 20 kg load cell indicated no output. Meanwhile, in terms of 50 g of calibration weight, the average output established by 5 kg and 20 kg load cell is W = 49.97033 and W = 50.42683. Therefore, 5 kg load cell is chosen to proceed for the fabrication of the torquemeter.
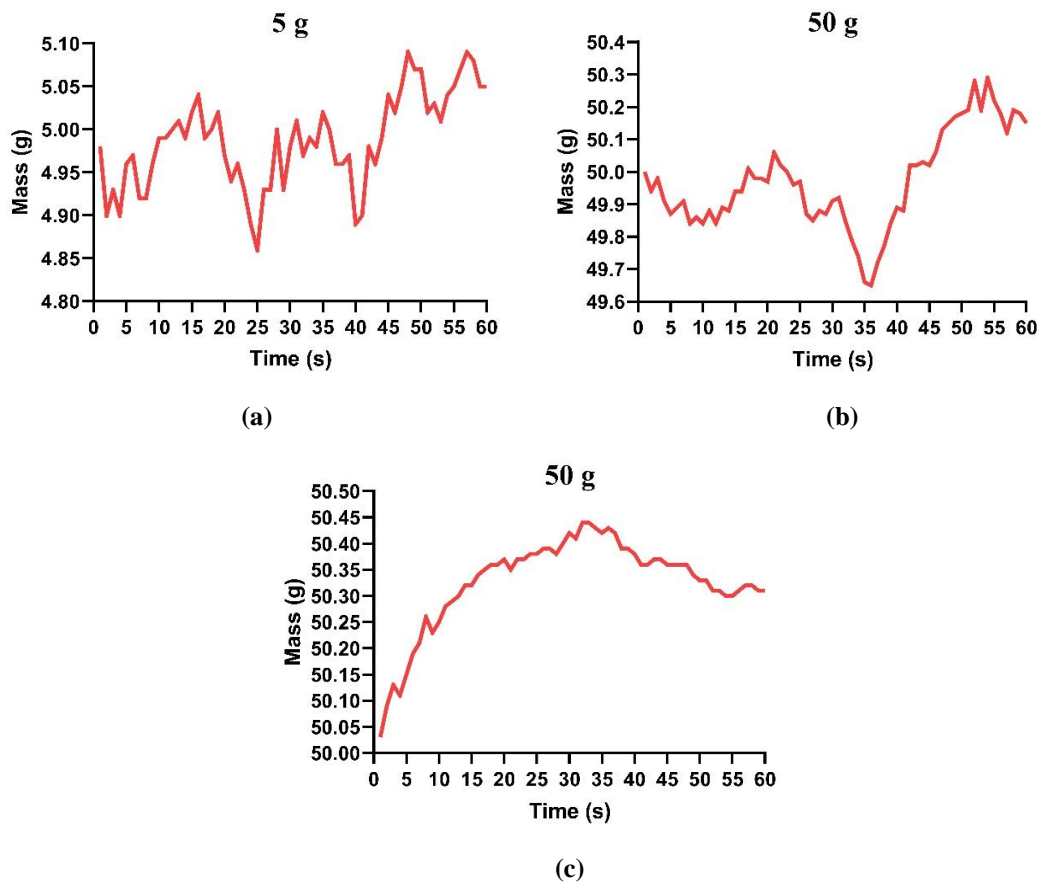

(a)

(b)

(c)

Fig. 5 - Output of 5 kg and 20 kg load cell output relative to defined load

The calibrated load cell secondary subsystem and primary photointerrupter subsystem is merged and interfaced in order to be coordinated by Arduino Mega 2560 as shown in Fig. 6. The microcontroller is powered by USB cable via PC for stable 5 V supply. The torque meter system is then evaluated with sketch code to execute both primary and secondary subsystem. However, in order to acquire force acting on load cell the WT shaft connector is attached with 3D printed fiction clamp as shown in Fig. 7. The geometrical attributes of the friction clamp are that it consists of two separate extruded frame arms from the center of the clamp. The stiffness of the clamp is with the wall of connector of the WT shaft is monitored via adjusting the intensity of the screw tightness. Since the friction clamp is 3D printed via FFF method, it is highly recommended to finish and smoothen the internal part of the clamp in order to remove excess flashes, surface roughness and irregularities. The friction clamp is tightened against the connector of the WT rotor at moderate intensity in order to provide grip and to reduce intense friction factor due to surface contact between two surfaces. The structure of the torquemeter code is established into two domains namely RPM acquisition and torque measurement. In regards to torque measurement domain, the force applied on the load cell is then multiple with the length from the center of rotation to the tip of the of the friction clamp. The complete configuration of DIY torquemeter

in WTL relative to WT system is shown in Fig. 8. Table 5 shows the list of components required for the fabrication of the torquemeter system.

Table 2 - List of components and specification for torquemeter

| Components	Role	Part number
Arduino	Microcontroller	Mega 2560
Photointerrupter	Non-contact optical type photosensor	GP1A57HRJ00F
Photointerrupter breakout board	Printed circuit board (PCB) for photo-interrupter	GP1A57HRJ00F
Resistor	220 Ω resistor for photo interrupter breakout board	-
Load cell amplifier	Amplifies electrical signal generated by load cell.	HX 711
LCD shield Arduino	Monitor display with access male pins for additional ground and V_{in} (5 V).	-
Load cell 1kg	Converters applied load to electrical signal, with rated capacity of 10 kg.	TAL 220B
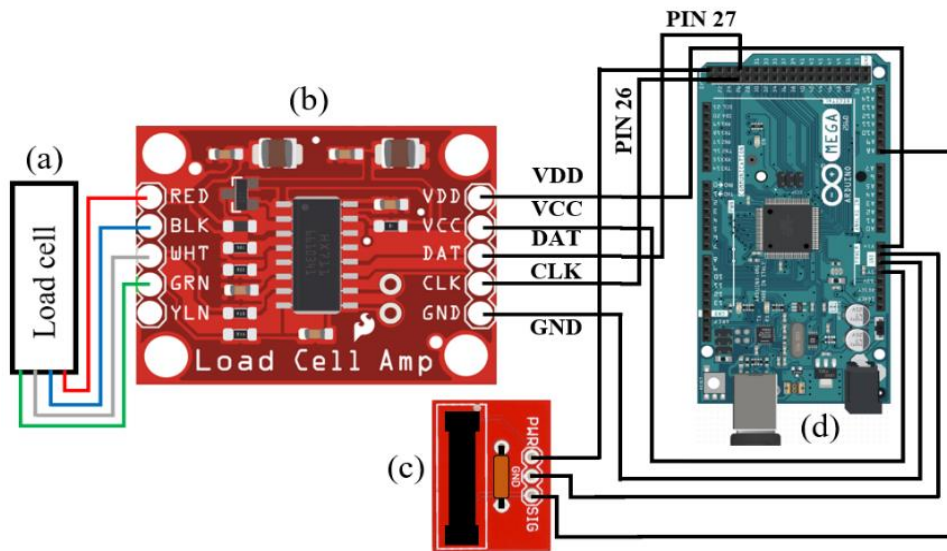
Fig. 6 - Torque meter schematic (a) straight bar load cell; (b) HX711 load cell amplifier; (c) photointerrupter; (d) Arduino Mega 2560
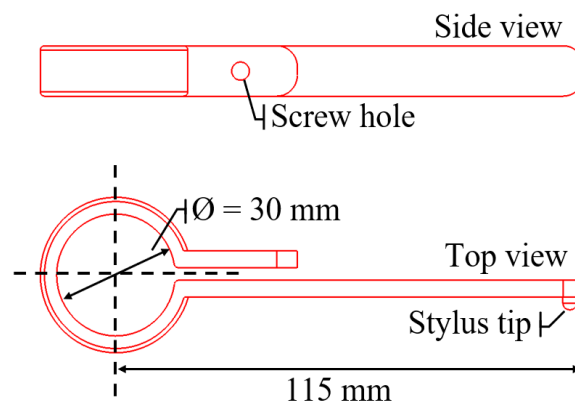

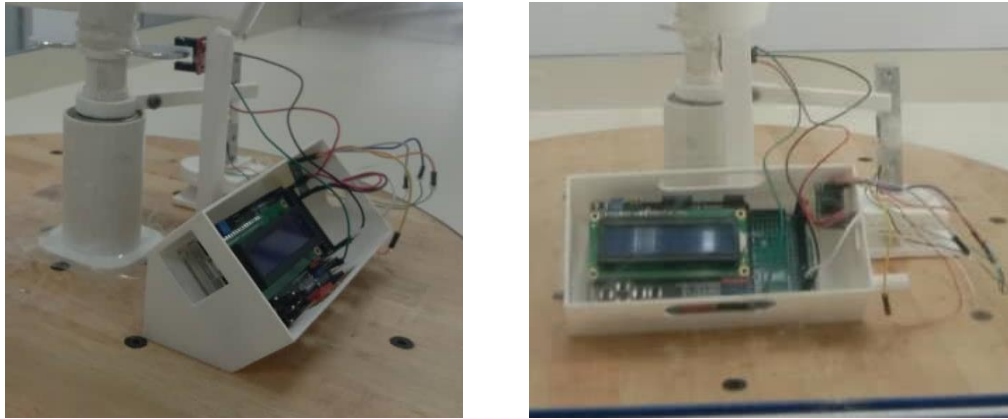**Fig. 7 - Friction clamp top and side view**

Fig. 8 - Torquemeter configuration in WTL

4. Result and Discussion

Calibration process works on the principal based on the solution given by a set of defined equations and also subjected to the design architecture of the instrument [42]. In order to further verify the sensitivity and linearity the load cell is examined under 3 different mases namely 10 g, 20 g and 100 g. Furthermore, to ensure the sensitivity of the calibration technique an average of 3 readings is collected of each mass subjected to the load cell. Moreover, the purpose of this process is to verify the linearity of strain gauge to the force applied. As shown in Fig. 9, 5 kg load cell exhibited unsteady noise behavior relative to the defined calibration weight at 1st trial. Although, HX711 ADC reading exhibited linear behavior relative to the respective calibration weight, the mass output relative to time response indicated unsteady behavior. This is due to the nature of load cell which is sensitive to changes in the environment. There are several environmental factors that influences the sensitivity of the load cell namely vibration, electrostatic, electromagnetic noise and temperature.

Moreover, in terms of the load cell itself the factors such as material, capacity range, sensitivity range and repeatability. Since the utilized load cell is made of aluminum alloy, the behavioral property of the material limits the accuracy of the measurement. It is observed that under constant load over a long period of time, the output voltage fluctuates due to deformation of the strain gauge and the counter reactive force induced by the structure of the load cell. Moreover, the fluctuations are obvious after 100 s, where prior to that a steady rise in output with minimal noise can be observed for all the weights. This phenomenon is also due to stress relaxation relative to time relaxation, where the stress applied by the load decreases due to the strain by the foil of strain gauge deformation. Besides, the changes in output voltage is due to the creeping effect of the load cell structure. The fluctuation and error are also due repeatability where sufficient time is not provided for the load cell for creep recovery relative to time relaxation and number of trials. The claim is support by research conducted by Bartel & Yaniv, (1997) [44], where similar recovery time as the tested time is required for load cell in order to prevent inaccuracy and creep effects. Table 3 reports the average load cell output acquired with different masses over time period of 900 s for 3 trials. Furthermore, Equation 9 - 11 is adapted to numerate the percentage of error and accuracy relative to the calibration technique. Results shows that, the percentage of error (P_e) of final 3th reading is P_e = 5.291 %, 2.68 %, 1.174 % for 10 g, 20 g and 100 g respectively. Meanwhile, the percentage of accuracy (P_a) of final 3th reading is P_a = 94.709 %, 97.32 %, 98.826 % for 10 g, 20 g and 100 g respectively.

Thereby, it is observed that the percentage of accuracy changes in response to magnitude of the load applied. This indicates that P_e and P_a is subjected to the nominal specification of the respective load cell. It is safe to say that sensitivity of the strain gauge load cell fluctuates relative to frequency of usage. Therefore, it is recommended to calibrate the load cell after every usage. Since the presented calibration technique indicated trivial dissimilarities under multiple verification, it is safe to say the secondary subsystem is calibrated. Meanwhile, effectiveness of the photointerrupter subsystem is examined under the influence wind speed of U_∞ = 5.1 m/s, 5.3 m/s, and 5.9 m/s relative to WT system. Fig. 10 shows the RPM result of the WT system measured via photointerrupter subsystem. The output of photointerrupter subsystem is verified against measurement acquired by tachometer. Error estimation analysis of the primary subsystem indicated the percentage of error is trivial and below 5 % which is an acceptable range of error in data acquisition as reported in Table 4.

The acquired data from the fabricated torquemeter system is verified against CFD simulation. For simplicity and to reduce computational time in analyzing the effectiveness of the system with regards to simulation, therefore the CFD numerical simulation is narrowed down to 2D configuration. In order to avoid biasness in investigating the effectiveness of the system, the numerical simulation configured similar to WTL procedure namely wind speed, domain

size and WT parametric attributes. Since the objective of this simulation is to verify the numerical values presented by the torquemeter system, therefore comprehensive CFD verification methodology namely grid topology and turbulent model sensitivity study is not conducted. The CFD numerical model is executed in Fluent based on RANS as numerical strategy and realizable k-ε for turbulent transport model. The type of boundary condition adapted is Neuman configuration. The computational WTL domain is defined with inlet boundary condition of $U_\infty = 7.1$ m/s. The outlet pressure is set to 0-pascal and the bounding wall is set to symmetry type. Table 5 reports the parameters adapted as the boundary condition for the rudimentary numerical simulation. In terms of grid configuration and motion of the rotating domain, sliding mesh method (SMM) is utilized as shown in Fig. 11. Result shows that the average computational moment coefficient (C_m) at 497 RPM and $\lambda = 0.95$ is $C_m = 0.73$.

The computational moment (M_t) value is numerated based on Equation 12 in which $M_t = 0.205$. Meanwhile, the data acquired from torquemeter is $M_t = 0.173$. The percentage of error of computational and instrumentational torque is 15.6 %. There are several factors that has influenced the reading. The major motivating factor is WIV and blockage factor. It is noticed that, components especially load cell consequently impacted the reading due to the vibration incurred by wind load. Moreover, the measurement is also impacted by the vibrating and unsteady auxiliary component such as friction clamp which is responsible for delivering the rotational force to the load cell. In addition, the CFD numerical model has over predicted moment value since it has compensated the high blockage factor (Br = 21.6 %) and external environmental factors. However, percentage of error can be minimized with use of algorithms to filter the noise spectrum. Besides, the error in measurement can be further minimized with the use of systematic load cell mechanism instead of foil-based load cell. However, it is safe to say, that the presented low-cost torque measuring instrument is applicable and feasible for WT. Table 6 reports the estimated error of the torquemeter in regards experimental WT system and CFD numerical model.
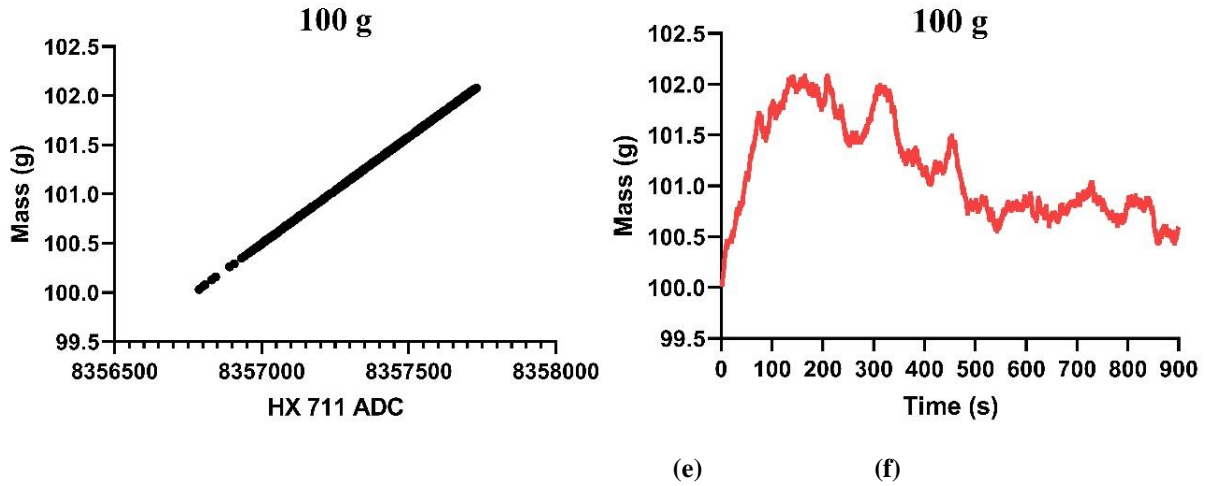

(a)   (b)

(b)   (d)

(e)　　　　　　　(f)
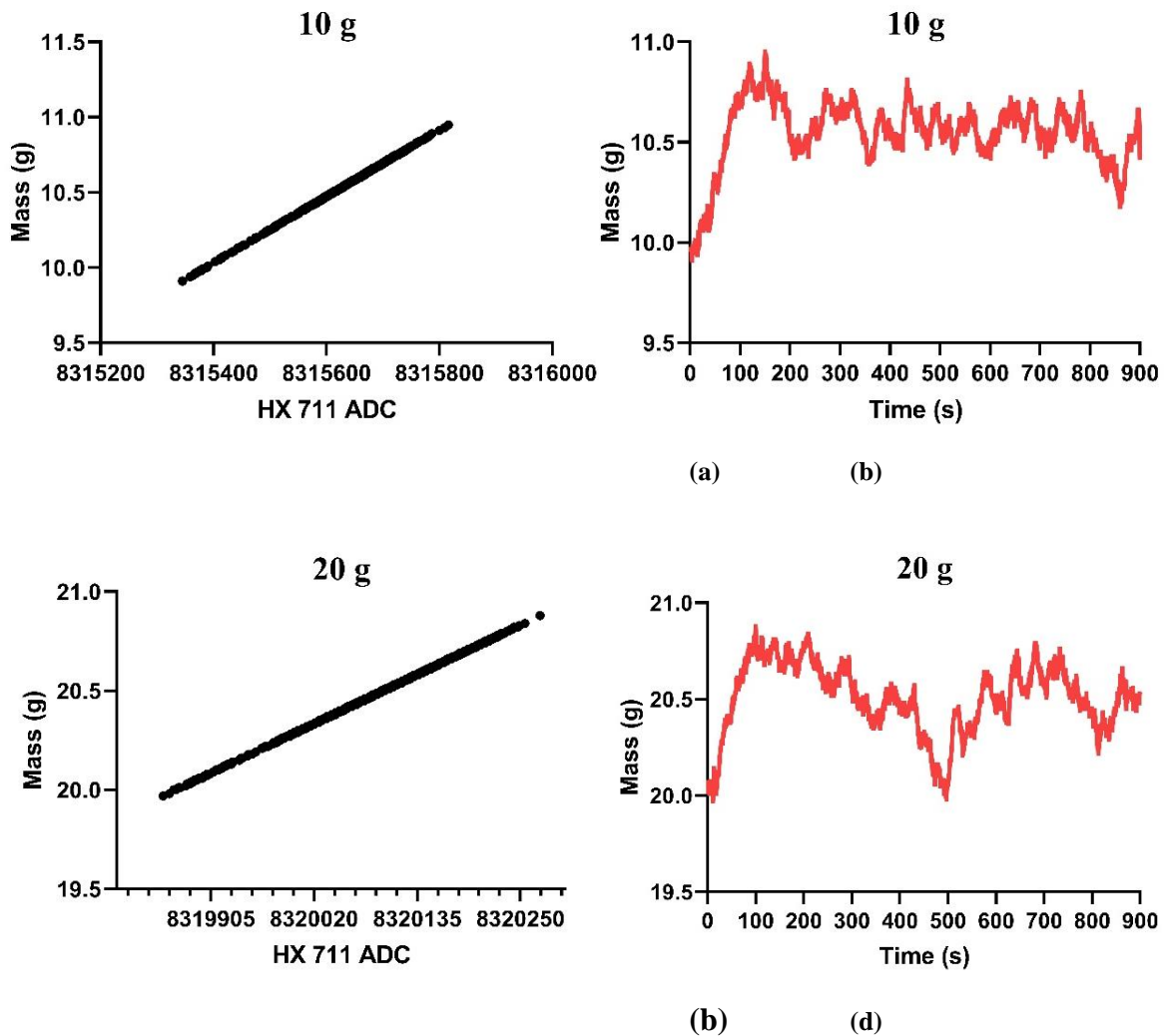
Fig. 9 - 5 kg load cell output (a) 10 g - HX 711; (b) 10 g – time; (c) 20 g - HX 711; (d) 20 g – time; (e) 100 g - HX 71; (f) 100 g – time

Table 3 - Average load cell output acquired with different masses at 3 trials

Average reading	Reading 1 (g)	Reading 2 (g)	Reading 3 (g)
10 g	10.5499	10.1182	10.5291
20 g	20.5427	20.5069	20.5351
100 g	101.0823	101.1421	101.1735

$$Relative\ error = \left| \frac{y_{Measure} - y_{true}}{y_{true}} \right| \qquad (9)$$

$$Error\ (\%) = Relative\ error \times 100 \qquad (10)$$

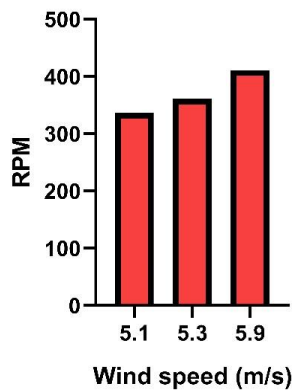$$Pecentage\ of\ accuracy\ (\%) = 100 - \%Error \qquad (11)$$

Fig. 10 - Comparison of RPM result by photointerrupter and tachometer

Table 4 - RPM values of photointerrupter subsystem and tachometer

Wind speed (m/s)	Photointerrupter system (RPM)	Tachometer (RPM)	Error (%)
5.1	337	342	1.483
5.3	361	370	2.432
5.9	411	421	2.433

Table 5 - CFD boundary condition parameters

Boundary condition	Parameter	Value

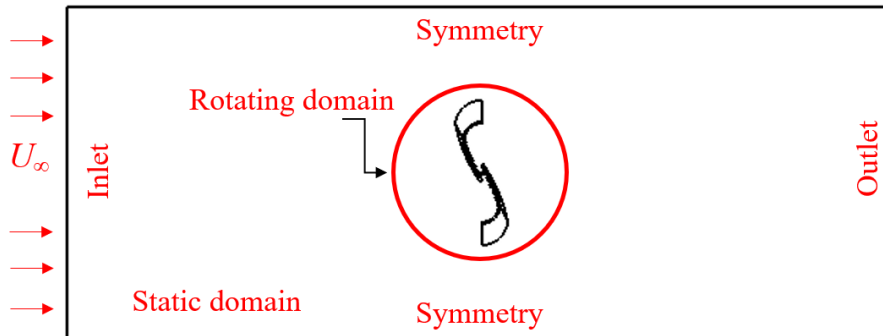| Boundary condition type	Neumann condition	Constant
Inlet	Constant velocity, U_∞	7.1 m/s
Surrounding wall type	Symmetry	-
Outlet	Pressure outlet	0-pascal gauge pressure

Fig. 11 - Computational domain of virtual WTL

$$C_m = \frac{M_t}{\frac{1}{4}\rho S_A D_r U_\infty^2} \qquad (12)$$

Table 6 - Error estimaiton of the torquemeter system and CFD numerical model

Parameter	CFD model	DIY torquemeter	Error estimation (%)
Moment	0.205	0.173	15.6

5. Conclusion

In this study, a low cost Arduino coordinated digital torquemeter is fabricated. The configuration of the torquemeter is designed for wind turbine torque assessment. The device is also being tested to confirm the system functionality. It is concluded that external factors have impacted the performance of the torquemeter system which consequently motivated the percentage of error of 11.35 % in contrast to torquemeter and CFD numerical model. However, the CFD numerical model has over predicted the moment value since it has compensated the blockage factor and external environmental factors. However, percentage of error can be minimized with use of algorithms to filter the noise spectrum. Besides, the error in measurement can be further minimized with the use of systematic load cell mechanism instead of foil-based load cell. It is safe to say, that the presented low-cost torque measuring instrument is applicable and feasible for WT torque assessment. As for future work further enhancement in terms of hardware configuration, sensitivity analysis design modification is required in order to improve the effectiveness and reliability of the torquemeter.

Acknowledgement

References

[1]   H. Sadat-Hosseini *et al.*, "CFD, system-based and EFD study of ship dynamic instability events: Surf-riding, periodic motion, and broaching," *Ocean Eng.*, vol. 38, no. 1, pp. 88–110, Jan. 2011, doi: 10.1016/j.oceaneng.2010.09.016.
[2]   T. Cebeci, *Numerical and Physical Aspects of Aerodynamic Flows*. Springer Berlin Heidelberg, 2014.
[3]   H. Hashimoto, T. Omura, A. Matsuda, S. Yoneda, F. Stern, and Y. Tahara, "Several remarks on EFD and CFD for ship roll decay," *Ocean Eng.*, vol. 186, no. January, p. 106082, Aug. 2019, doi: 10.1016/j.oceaneng.2019.05.064.
[4]   P. Šafařík, "Experimental Investigation in Fluid Mechanics – Its Role, Problems and Tasks," in *EPJ Web of Conferences*, Apr. 2013, vol. 45, p. 01118, doi: 10.1051/epjconf/20134501118.

[5]   P. Mohazzab, "Archimedes' Principle Revisited," *J. Appl. Math. Phys.*, vol. 05, no. 04, pp. 836–843, 2017, doi: 10.4236/jamp.2017.54073.

[6]   M. Ožvoldová, P. Špiláková, and L. Tkáč, "Archimedes' principle-internet accessible remote experiment," *Int. J. Interact. Mob. Technol.*, vol. 10, no. 5, pp. 36–42, 2014, doi: 10.3991/ijoe. v10i5.3831.

[7]   T. G. Chondros, "Archimedes Influence in Science and Engineering," in *The Genius of Archimedes -- 23 Centuries of Influence on Mathematics, Science and Engineering*, 2010, pp. 411–425.

[8]   D. Jackson and B. Launder, "Osborne Reynolds and the Publication of His Papers on Turbulent Flow," *Annu. Rev. Fluid Mech.*, vol. 39, no. 1, pp. 19–35, 2007, doi: 10.1146/annurev.fluid.39.050905.110241.

[9]   J. D. Jackson, "Osborne Reynolds: Scientist, Engineer and Pioneer," in *Proceedings: Mathematical and Physical Sciences*, Jun. 1995, vol. 451, no. 1941, pp. 49–86, [Online]. Available: http://www.jstor.org/stable/52793.

[10]   A. Nur, R. Afrianita, and R. D. T. F. Ramli, "Effect of pipe diameter changes on the properties of fluid in closed channels using Osborne Reynold Apparatus," in *IOP Conference Series: Materials Science and Engineering*, Sep. 2019, vol. 602, no. 1, p. 012058, doi: 10.1088/1757-899X/602/1/012058.

[11]   K. Arnold, "Pascal's Great Experiment," *Dialogue Can. Philos. Assoc.*, vol. 28, no. 3, pp. 401–416, Apr. 1989, doi: 10.1017/S0012217300015936.

[12]   W. E. K. Middleton, "The Place of Torricelli in the History of the Barometer," *Isis*, vol. 54, no. 1, pp. 11–28, Jun. 1963, [Online]. Available: http://www.jstor.org/stable/228726.

[13]   A. Chodos, "This Month in Physics History: Torricelli Demonstrates the Existence of a Vacuum," *APS News*, 2012. https://www.aps.org/publications/apsnews/201210/physicshistory.cfm (accessed Jun. 10, 2020).

[14]   V. R. Aggarwal, S. Kumar, B. Paosawatyanyong, and P. Wattanakasiwich, "Safe Torricelli Experiment for Educational use in a Science Resource Center," in *AIP Conference Proceedings*, Jul. 2010, vol. 1263, no. 1, pp. 91–93, doi: 10.1063/1.3479901.

[15]   A. N. Abdul Ghani, "Experimental Research Methods for Students in Built Environment and Engineering," in *MATEC Web of Conferences*, Mar. 2014, vol. 10, p. 01001, doi: 10.1051/matecconf/20141001001.

[16]   S. A. N. van Riesen, H. Gijlers, A. A. Anjewierden, and T. de Jong, "The influence of prior knowledge on the effectiveness of guided experiment design," *Interact. Learn. Environ.*, vol. 0, no. 0, pp. 1–17, Jun. 2019, doi: 10.1080/10494820.2019.1631193.

[17]   Y. Ma, S. Xie, X. Zhang, and Y. Luo, "Hybrid calibration method for six-component force/torque transducers of wind tunnel balance based on support vector machines," *Chinese J. Aeronaut.*, vol. 26, no. 3, pp. 554–562, Jun. 2013, doi: 10.1016/j.cja.2013.04.056.

[18]   G. Zhang, D. Zappalá, C. Crabtree, C. Donaghy-Spargo, S. Hogg, and A. Duffy, "Validation of a non-contact technique for torque measurements in wind turbines using an enhanced transient FSV approach," *Measurement*, vol. 151, p. 107261, Feb. 2020, doi: 10.1016/j.measurement.2019.107261.

[19]   B. Liu, H. Gao, K. Zhao, J. Huang, and Y. Sun, "A new design of a support force measuring system for hypersonic vehicle aerodynamic measurement," *Flow Meas. Instrum.*, vol. 70, p. 101646, Dec. 2019, doi: 10.1016/j.flowmeasinst.2019.101646.

[20]   M. D. Atkins and M. F. Boer, "Flow Visualization," in *Application of Thermo-Fluidic Measurement Techniques*, T. Kim, T. J. Lu, and S. J. B. T.-A. of T.-F. M. T. Song, Eds. Elsevier, 2016, pp. 15–59.

[21]   N. Gao and X. H. Liu, "An improved smoke-wire flow visualization technique using capacitor as power source," *Theor. Appl. Mech. Lett.*, vol. 8, no. 6, pp. 378–383, Dec. 2018, doi: 10.1016/j.taml.2018.06.010.

[22]   A. Sciacchitano, G. C. A. Caridi, and F. Scarano, "A Quantitative Flow Visualization Technique for On-site Sport Aerodynamics Optimization," *Procedia Eng.*, vol. 112, pp. 412–417, 2015, doi: 10.1016/j.proeng.2015.07.217.

[23]   K. Ghorbanian, M. R. Soltani, and M. D. Manshadi, "Experimental investigation on turbulence intensity reduction in subsonic wind tunnels," *Aerosp. Sci. Technol.*, vol. 15, no. 2, pp. 137–147, Mar. 2011, doi: 10.1016/j.ast.2010.06.009.

[24]   T. Maeda *et al.*, "Wind tunnel study on wind and turbulence intensity profiles in wind turbine wake," *J. Therm. Sci.*, vol. 20, no. 2, pp. 127–132, Jun. 2011, doi: 10.1007/s11630-011-0446-9.

[25]   Y. He, J. Cheung, Q. Li, and J. Fu, "Accurate determination of reference wind speed and reference static pressure in wind tunnel tests," *Adv. Struct. Eng.*, vol. 23, no. 3, pp. 578–583, Feb. 2020, doi: 10.1177/1369433219875302.

[26]   X. Wang, X. Wang, X. Ren, X. Yin, and W. Wang, "Effects of tube system and data correction for fluctuating pressure test in wind tunnel," *Chinese J. Aeronaut.*, vol. 31, no. 4, pp. 710–718, Apr. 2018, doi: 10.1016/j.cja.2018.01.021.

[27]   R. Pérez Ubeda, S. C. Gutiérrez Rubert, R. Zotovic Stanisic, and Á. Perles Ivars, "Design and Manufacturing of an Ultra-Low-Cost Custom Torque Sensor for Robotics," *Sensors*, vol. 18, no. 6, p. 1786, Jun. 2018, doi: 10.3390/s18061786.

[28]   P. Yadav, M. Pant, A. Sheoran, P. Kumar Arora, and H. Kumar, "Design and Fabrication of low capacity Torque Transducer," *IOP Conf. Ser. Mater. Sci. Eng.*, vol. 748, p. 012032, Feb. 2020, doi: 10.1088/1757-899X/748/1/012032.

[29]   M. Kunimatsu, "Measurement of dynamic pressure using piezoelectric sensors at extremely low temperatures," *JSAE Rev.*, vol. 22, no. 4, pp. 553–558, Oct. 2001, doi: 10.1016/S0389-4304(01)00133-3.

[30]   R. Robey, "Blast Tubes," in *Handbook of Shock Waves*, G. BEN-DOR, O. IGRA, and T. O. V. B. T.-H. of S. W. ELPERIN, Eds. Burlington: Elsevier, 2001, pp. 623–650.

[31]   A. Boutemedjet, M. Samardžić, D. Ćurčić, Z. Rajić, and G. Ocokoljić, "Wind tunnel measurement of small values of rolling moment using six-component strain gauge balance," *Measurement*, vol. 116, pp. 438–450, Feb. 2018, doi: 10.1016/j.measurement.2017.11.043.

[32]   H. M. Şahin and M. Saim Soysal, "Development of an air velocity and flow measurement system by using a novel circular disc," *Flow Meas. Instrum.*, vol. 78, p. 101890, Apr. 2021, doi: 10.1016/j.flowmeasinst.2021.101890.

[33]   C. Wang, P. Mi, Z. Tian, and G. Yi, "Study on temperature characteristics and correction of strain gauge balance in actual airflow environment," *Aerosp. Sci. Technol.*, vol. 106, p. 106201, Nov. 2020, doi: 10.1016/j.ast.2020.106201.

[34]   K. Jiang, Y. Zhou, L. Han, L. Li, Y. Liu, and S. Hu, "Design of a High-Resolution Instantaneous Torque Sensor based on the Double-Eccentric Modulation Principle," *IEEE Sens. J.*, vol. 19, no. 16, pp. 1–1, 2019, doi: 10.1109/JSEN.2019.2911392.

[35]   D. Zappalá, M. Bezziccheri, C. J. Crabtree, and N. Paone, "Non-intrusive torque measurement for rotating shafts using optical sensing of zebra-tapes," *Meas. Sci. Technol.*, vol. 29, no. 6, p. 065207, Jun. 2018, doi: 10.1088/1361-6501/aab74a.

[36]   A. J. Hebra, "Force, mass, weight, and torque," in *The Physics of Metrology*, A. J. Hebra, Ed. Vienna: Springer Vienna, 2010, pp. 93–113.

[37]   A. S. Morris and R. Langari, "Mass, Force, and Torque Measurement," in *Measurement and Instrumentation*, A. S. Morris and R. B. T.-M. and I. (Second E. Langari, Eds. Boston: Elsevier, 2016, pp. 547–564.

[38]   R. Semiconductor, "Optical Sensors 2011," 2011.

[39]   J. Bernhard, "What matters for students' learning in the laboratory? Do not neglect the role of experimental equipment!," *Instr. Sci.*, vol. 46, no. 6, pp. 819–846, Dec. 2018, doi: 10.1007/s11251-018-9469-x.

[40]   K. N. Choi, "Noise in Load Cell Signal in an Automatic Weighing System Based on a Belt Conveyor," *J. Sensors*, vol. 2017, no. 1, pp. 1–9, 2017, doi: 10.1155/2017/1524782.

[41]   J. . Joo, K. . Na, and D. . Kang, "Design and evaluation of a six-component load cell," *Measurement*, vol. 32, no. 2, pp. 125–133, Sep. 2002, doi: 10.1016/S0263-2241(02)00002-7.

[42]   J. G. Rocha, C. Couto, and J. H. Correia, "Smart load cells: an industrial application," *Sensors Actuators A Phys.*, vol. 85, no. 1–3, pp. 262–266, Aug. 2000, doi: 10.1016/S0924-4247(00)00415-5.

[43]   T. Jaysrichai, "Load Cells Application for Developing Weight-Bearing Detection via Wireless Connection," *Open Biomed. Eng. J.*, vol. 12, no. 1, pp. 101–107, Nov. 2018, doi: 10.2174/1874120701812010101.

[44]   T. W. Bartel and S. L. Yaniv, "Creep and creep recovery response of load cells tested according to US and international evaluation procedures," *J. Res. Natl. Inst. Stand. Technol.*, vol. 102, no. 3, p. 349, May 1997, doi: 10.6028/jres.102.024.